Chapter 4

Low temperature Synthesis, dielectric and electrical characteristics of $Bi_{2/3}Cu_{3-x}Ni_xTi_4O_{12}$ (where x=0.05, 0.1, and 0.2) ceramics for the dielectric and electrical properties

Low temperature Synthesis, dielectric and electrical characteristics of $Bi_{2/3}Cu_{3-x}Ni_xTi_4O_{12}$ (where x=0.05, 0.1, and 0.2) ceramics for the dielectric and electrical properties

4.1. Introduction

There is a continuous effort to downsize electronic devices such as dynamic random-access memory and multilayer ceramic capacitors to reduce the size and cost by investigating materials with giant dielectric-constant [1-6]. A variety of materials have been investigated in the past two decades, including $BaTiO_3$, NiO, $SrTiO_3$, $CaCu_3Ti_4O_{12}$ (CCTO), and TiO_2 [7,8]. Among all ceramics, the dielectric performance of CCTO has shown an extremely high dielectric constant. This system can be further improved and properties can be greatly enhanced by cation doping and substitution. CCTO class of materials have an extraordinarily high dielectric constant $\varepsilon_r \sim 10^4$–10^5 and show good thermal stability in a wide temperature range from 100 K to 600 K and broad frequency region (10^2-10^7 Hz). It has great potential for electronic components such as multilayer capacitors and electrical devices due to its high dielectric constant. Doping has proven to be a useful way to improve loss and performance. The dielectric characteristics and the microstructure have a strong correlation [9,10]. The ionic size and nature (acceptor/donor) of the dopant play a significant role in controlling the microstructure and dielectric properties of CCTO ceramic [11]. Because of the correction of the mixed-valent structure, partial isovalent ion substitution of Zr, Zn, and Y in CCTO ceramics enriched the dielectric response. For the wide application of this compound further improvement in the dielectric loss is needed. Several theories have been proposed to explain the source of high dielectric constant and low dielectric loss. Some of these mechanisms involve the internal domain, electrode polarization effect, bimodal grain size model, and the internal barrier layer concept (IBLC) [12-18]. The Internal Barrier

Layer Capacitance (IBLC) model has been accepted to be reliable for explaining high dielectric constant and loss in the material. This mechanism assumes that polycrystalline compounds are made up of semiconducting grains separated by insulating grain boundaries [19,20]. Microstructural features are very important in explaining the IBLC model. As a result, the dielectric permittivity of CCTO ceramics can be altered by fine-tuning their microstructure via processing parameters and/or metal ion doping [22,23]. The high permittivity exhibited in this class of compounds has been also explained based on the Maxwell–Wagner (M–W) relaxation mechanism associated with an interfacial polarization, which appears in electrically heterogeneous materials (grains enclosed by grain boundaries of different conductivity) [21]. This has been supported by impedance spectroscopy and revealed that the perovskite material has insulating grain boundaries that separate the semiconducting grains, similar to a single-step internal barrier layer capacitor. The isostructural relationship between $Bi_{2/3}Cu_3Ti_4O_{12}$ (BCTO) and CCTO has already been documented in the literature. Yang et al. employed a solid-state reaction method and synthesized BCTO, and reported a dielectric constant of approximately 3.3 x 10^5 at 1 kHz [23]. We have used a cost-effective chemical method to synthesize Ni-doped $Bi_{2/3}Cu_3Ti_4O_{12}$ (BCNTO) ceramics at relatively low temperatures and measured their microstructural, dielectric, and electrical properties. These results are discussed using current mechanisms for high dielectric constant.

4.2. Materials synthesis and characterization

A low-temperature low cost chemical synthetic process was used for $Bi_{2/3}Cu_{3-x}Ni_xTi_4O_{12}$ (where x= 0.05, 0.1, and 0.2)ceramics. The ceramics were termed as BCNTO-0.05, BCNTO-0.1 and BCNTO-0.2 for x= 0.05, 0.1 and 0.2, respectively. In this synthesis, Bismuth nitrate $Bi(NO_3)_3.5H_2O$ (99% Merck, India), Copper acetate $Cu(CH_3COO)_2.H_2O$ (99% Merck, India), Nickel Nitrate $Ni(NO_3)_2.6H_2O$ (99% Merck, India), and Titanium oxide TiO_2(98.5% Merck, India) were used as the source materials. These source materials were mixed in the equivalent ratio. The solution of $Bi(NO_3)_3.5H_2O$, $Cu(CH_3COO)_2.H_2O$, and $Ni(NO_3)_2.6H_2O$ was prepared by dissolving in the distilled water. Then The solid TiO_2 was added to the solution. As a chelating agent, the stoichiometric quantity of citric acid (99.5 %, Merck India) prepared solution in the distilled water was added to the solution. In the ignition process, citric acid was also used as a fuel. The resulting solution was heated at 343-353 K on a hotplate. A magnetic stirrer was used for the mixing of solution as well as for evaporation of some gases. A fluffy mass of BCNTO powders was recovered after eliminating a substantial amount of gas. The obtained BCNTO particles were pulverized into a fine powder using a pestle and mortar. The powders were calcined for 8 h at 1073 K. Using calcined powders and 2% PVA as a binder, cylindrical pellets were made using a hydraulic press at 5 tons of pressure for 90 s. This binder was burned out for 3 h at 773 K. Finally, these BCNTO pellets were sintered for 8 h at 1123 K.

The crystalline phase of sintered material was characterized by X-ray Diffractometer (XRD) (Rigaku miniflex 600, Japanusing CuKα radiation waves, λ = 1.54059 Å).The elemental

analysis and microstructure of all samples were examined by Scanning Electron Microscope model EVO–18 research from ZEISS from Germany and Energy-Dispersive X-ray spectroscopy, supplied by Oxford instrument, respectively. Transmission electron microscopy, model FEI Tecnai-20G. 20 kV accelerating voltage was used to determine the bright-field TEM morphology. X-ray Photoelectron Spectroscopy was used to determine composition. The sintered pellets were polished on both sides and care was taken to make parallel surfaces. The silver paste was used as an electrode on both faces for the electrical and dielectric measurements. An LCR meter, model PSM 1735-NumetriQ, supplied by Newton 4th Ltd.UK was used for the dielectric measurements for the temperature range of 300 K to 500 K. The data was taken for the frequency range of 100 Hz to 10 MHz.

cyclic voltammetry (CV), charge-discharge (CD), electrochemical impedance spectroscopy (EIS) of the three and two-electrode systems were performed by Versastat 3. In a three-electrode system, Ag/AgCl, Pt, and active material were taken as reference electrodes, counter electrodes, and working electrodes respectively. The mass loading of the working electrode was 2 mg/cm^2. For Electrochemical Impedance Spectroscopy (EIS), 10 mV amplitude of AC voltage was applied over 100 kHz – 0.01 Hz frequency. For all the Electrochemical analyses, 1M KOH electrolyte was taken. Copper wire was taken as the current collector and a substrate (carbon paper) was attached to the copper wire with the help of conductive silver glue. The backside of the carbon paper and the exposed part of the copper wire was insulated by using gluestick. Then a dispersion was prepared to have 5 mg of prepared material, 2-propanol of 0.2 mL, Nafion of 12 µL, and drop cast on the carbon

paper of 1 cm^2 area. The active mass loading was 2 mg/cm^2. The scan rate was 5 mV/s. Then the prepared electrode was dried for around half an hour in a vacuum oven till the complete disappearance of the used solvents.

4.3. Results and discussion

4.3.1. X-ray Diffraction (XRD)

Fig. 4.1 shows the X-ray diffraction pattern of Ni-doped Bismuth Copper Titanium Oxide ($Bi_{2/3}Cu_{3-X}Ni_xTi_4O_{12}$, x= 0.05, 0.1, and 0.2) respectively. It is observed that the XRD pattern of the ceramic is very much similar to undoped BCTO ceramic (JCPDS card no. 46-0725), which confirms the single-phase formation. The primary XRD peaks of these ceramics were comparable to the planes (2 0 0), (2 1 1), (2 2 0), (3 1 0), (2 2 2), (3 2 1), (4 0 0), (4 2 2), and (4 4 0), and were found to be the similar as CCTO (JCPDS card no. 21-0140). The average crystallite size was calculated to be 42.07 nm, 42.08 nm, and 42.10 nm for BCNTO-0.05, BCNTO-0.1, and BCNTO-0.2 ceramics, respectively. The Debye-Scherrer's formula given below was used to determine the crystallite size of Ni-doped BCTO

$$D = \frac{k\lambda}{\beta cos\theta} \qquad (4.1)$$

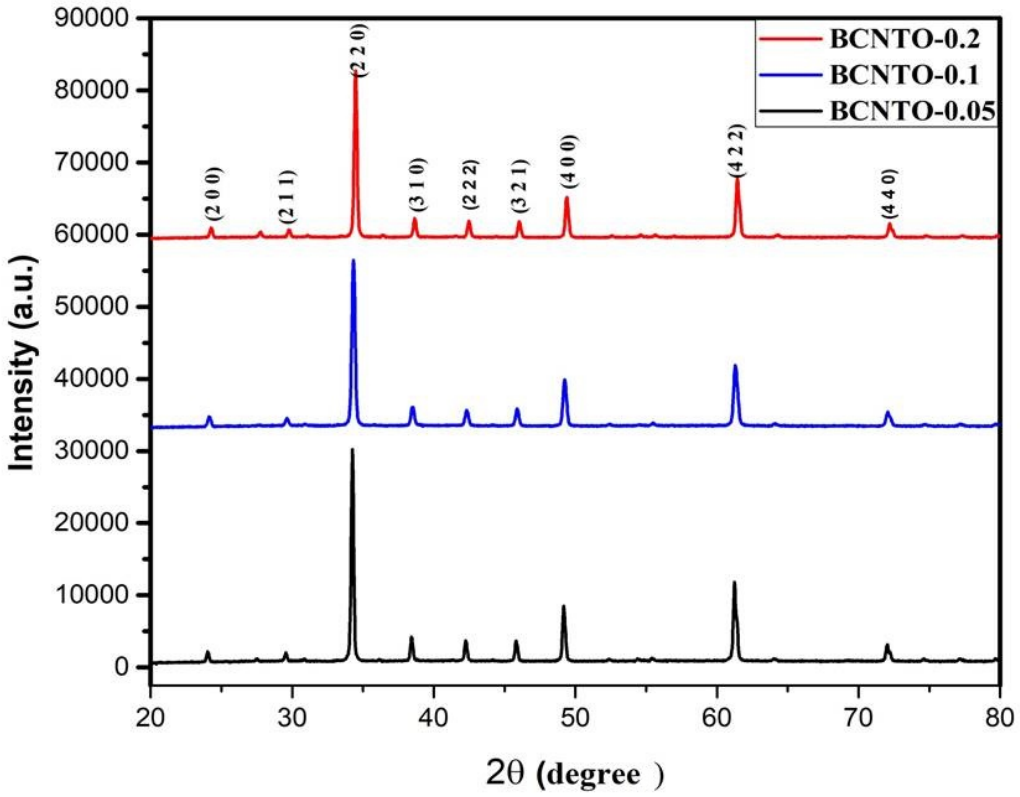

Fig. 4.1. XRD Pattern of BCNTO-0.05, BCNTO-0.1, and BCNTO-0.2 ceramics sintered at 1123 K for 8 h.

Where k= 0.89 is the crystal form coefficient,λ is the XRD wavelength, β is the Full-Width Half Maximum (FWHM), and θ is the diffraction angle. The crystal structure of the material was found to be body centered cubic (bcc).The lattice parameter (a) of BCNTO-0.05, BCNTO-0.1, and BCNTO-0.2 ceramic were calculated and found to be 7.393Å, 7.389 Å, and 7.363 Å respectively from XRD data. The volume of the unit cell is calculated to be

404.076 $Å^3$, 403.420 $Å^{3,}$ and 399.178 $Å^3$ for BCNTO-0.05, BCNTO-0.1, and BCNTO-0.2 ceramic.

4.3.2. Microstructural studies

4.3.2.1. Scanning Electron Microscopic (SEM) studies

The SEM morphologies are shown in Fig. 4.2a-c for BCNTO-0.05, BCNTO-0.1, and BCNTO-0.2 ceramics sintered at 1123 K for 8 h respectively. SEM images show surface morphology and surface characteristics of the samples. The average grain size of BCNTO-0.05, BCNTO-0.1, and BCNTO-0.2 ceramics are observed to be 0.43 μm, 0.39μm, and 0.41μm respectively. It clears from the figure that grains exist in granular form with the polygonal shape which is well parted by grain boundaries. Fig. 4.3a–c shows the Energy-Dispersive X-ray spectra (EDX) of the BCNTO-0.05, BCNTO-0.1, and BCNTO-0.2 ceramics, which agree with the presence of Bi, Cu, Ti, Ni, Ti, and O elements.

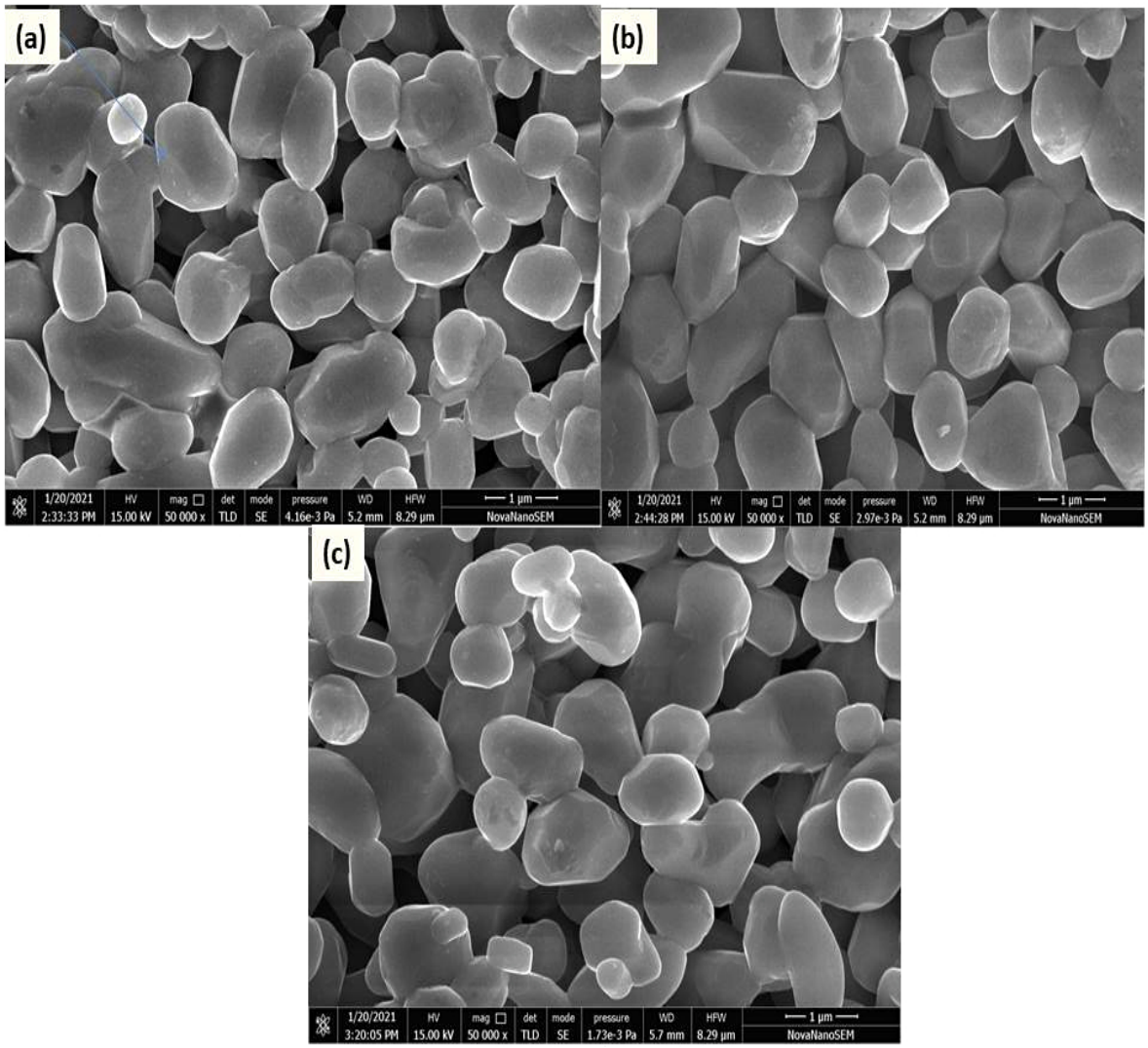

Fig. 4.2 SEM images of **a** BCNTO-0.05; **b** BCNTO-0.1; **c**BCNTO-0.2 ceramics sintered at 1123 K for 8 h.

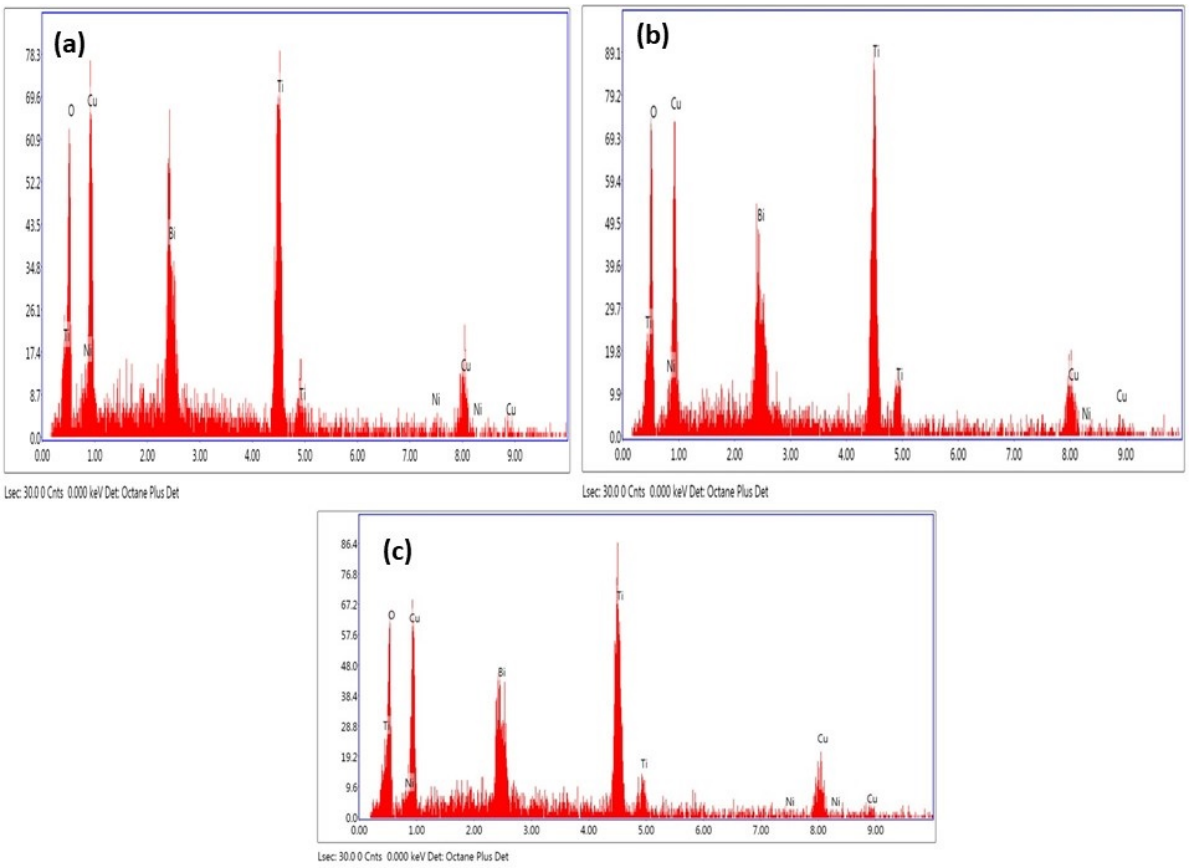

Fig. 4.3 EDX spectra of **a** BCNTO-0.05; **b** BCNTO-0.1; **c** BCNTO-0.2 ceramics sintered at 1123 K for 8 h.

4.3.2.2. Transmission Electron Microscopic (TEM) studies

Fig. 4.4a–c shows the bright-field TEM images of BCNTO-0.05, BCNTO-0.1, and BCNTO-0.2 ceramics sintered at 1123 K for 8 h respectively. The average particle sizes were found to be 52.01 nm, 56.44 nm, and 65.28 nm for BCNTO-0.05, BCNTO-0.1, and BCNTO-0.2 ceramics respectively. Fig. 4.4d-f depicts the Selected Area Electron Diffraction (SAED) pattern of BCNTO-0.05, BCNTO-0.1, and BCNTO-0.2 ceramics respectively. We have

shown the crystal plane of the SAED pattern of the ceramic. The existence of a few clear rings with small dots in the SAED pattern shows the formation of crystalline Ni-doped BCTO ceramic.

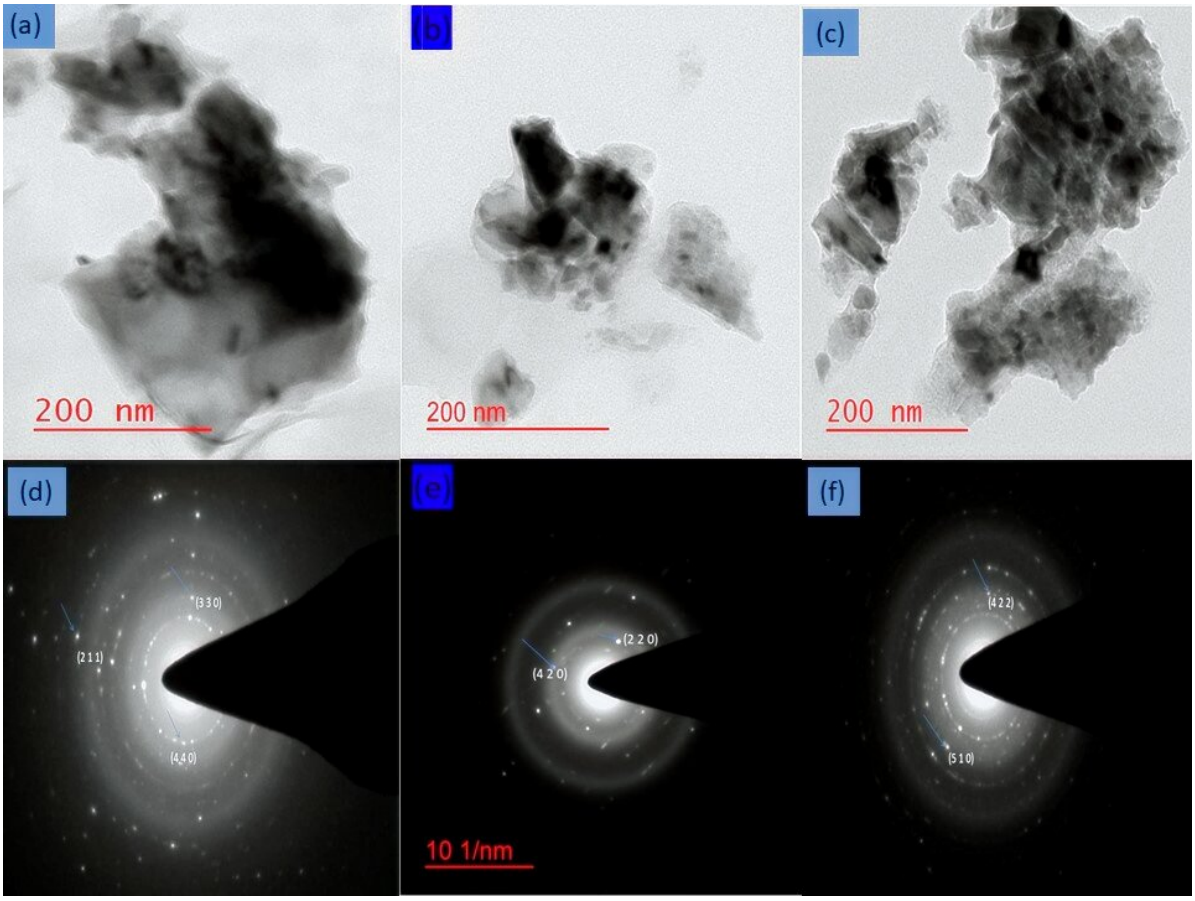

Fig. 4.4 a-c TEM images and **(d-f)** SAED pattern of BCNTO-0.05, BCNTO-0.1, and BCNTO-0.2 ceramics sintered at 1123 K for 8 h respectively.

4.3.3. X-Ray Photoelectron Spectroscopic (XPS) studies

XPS spectra of $Bi_{2/3}Cu_{3-x}Ni_xTi_4O_{12}$ (x=0.2) ceramic is presented in Fig. 4.5. Fig.4. 5a indicates the XPS spectrum of Bi, having Binding Energy (B.E.) 158.71 eV and 164.01 eV

were obtained for the states $^4f_{5/2}$ and $^4f_{7/2}$. This result indicates the existence of bismuth ion in the +3 oxidation state. The binding energy of copper-related to Cu ^2p spectra at the peak of 933.98 eV and 953.95 eV belonging to $^2p_{3/2}$ and $^2p_{1/2}$ respectively, confirms the presence of +2 oxidation state of Cu as shown in Fig. 4.5b [17, 24]. The XPS spectra of Ni, Ti, and O, shown in Fig. 4.5c, d, e, confirms the presence of oxidation states of +2, +4, and -2 respectively in the ceramic, which was confirmed by XPS studies [18].

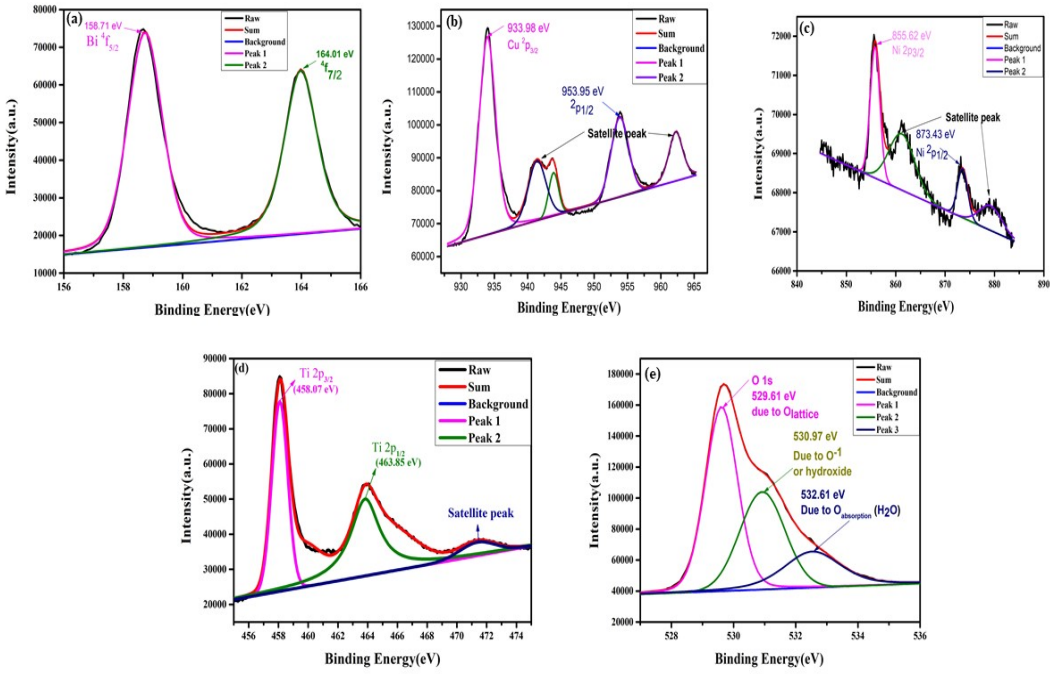

Fig. 4.5 XPS spectra of **a** Bi;**b** Cu;**c** Ni;**d**Ti;**e** O of BCNTO-0.2 ceramic sintered at 1123 K for 8 h.

4.3.4. Dielectric studies

Fig. 4.6a shows the measured data on the frequency dependence of the dielectric constant ε_r for sintered Ni-doped BCTO ceramics sintered at 1123 K for the period of 8 h. The values of ε_r for BCNTO-0.05, BCNTO-0.1, and BCNTO-0.2 ceramics measured at the temperature 470 K and 100 Hz, were found to be 852, 1352, and 1940 respectively.

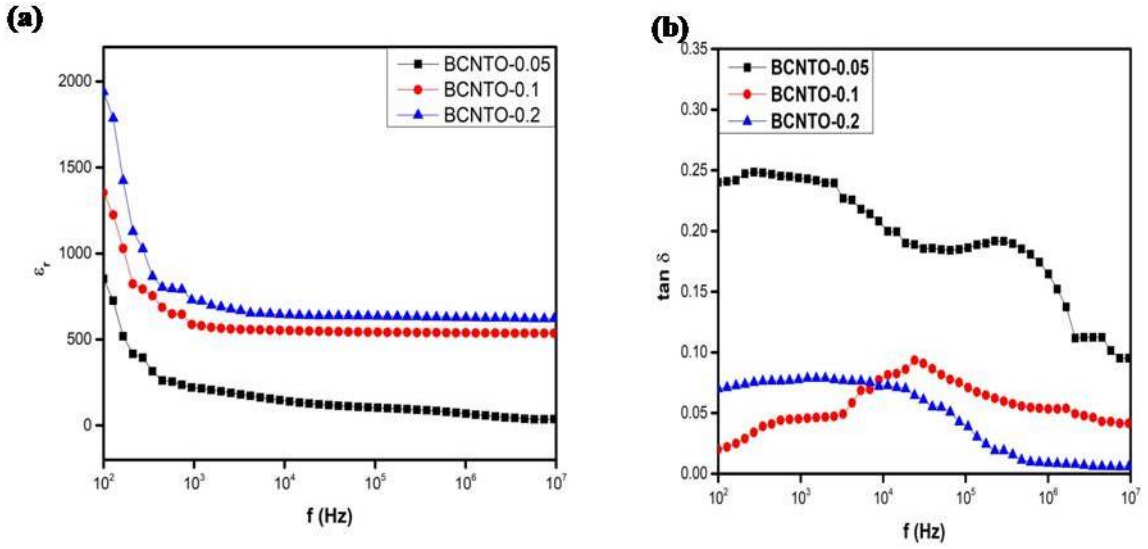

Fig. 4.6 Frequency dependence of **a** dielectric constant(ε_r) at 470 K; **b** dielectric loss (tan δ) for BCNTO-0.05, BCNTO-0.1, and BCNTO-0.2 ceramics at 310 K.

As seen in Fig. 4.6a, the dielectric constant (ε_r) drops fast in the lower frequency range while remaining constant in the higher frequency range. The value of tan δ is shown as a function of frequency. It declines smoothly in higher frequency regions, as seen in Fig. 4.6b. At 310 K and 10 kHz, The dielectric losses of BCNTO-0.05, BCNTO-0.1, and BCNTO-0.2 ceramics were determined to be 0.21, 0.08, and 0.07 respectively. As the Ni content

increases, the dielectric constant increases, and dielectric loss decreases due to the conductivity decreasing.

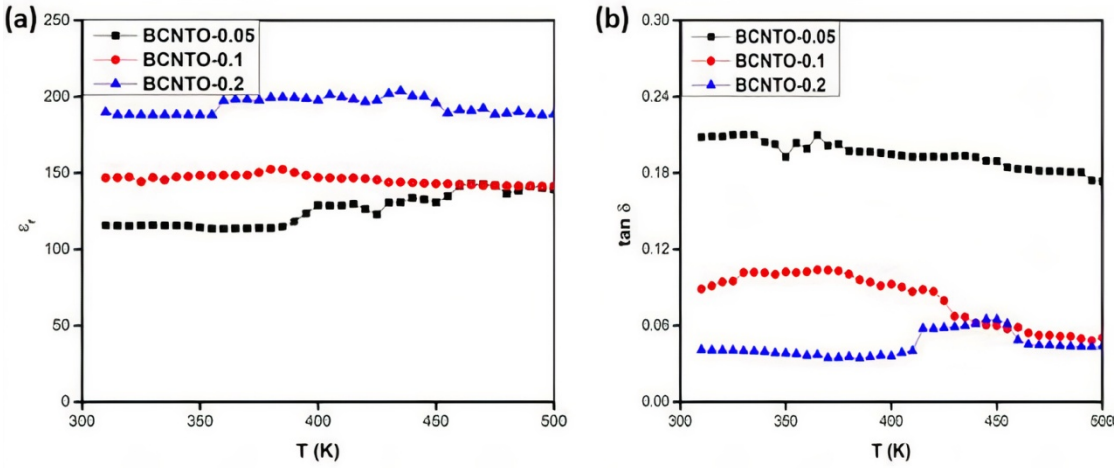

Fig. 4.7 Temperature dependence of **a** dielectric constant(ε_r); **b** tangent loss (tan δ) of BCNTO-0.05, BCNTO-0.1 and BCNTO-0.2 ceramics at 10 kHz.

Fig. 4.7a and 4.7b show the variation of ε_r and tangent loss as a function of temperature for the applied frequency of 10 kHz. The value of ε_r and tangent loss grows at first, reaches a maximum, and then gradually drops to a smaller value, as seen in the graph. Both show a reduction until becoming practically self-sufficient. This type of behavior can be explained based on the space charge model of Maxwell-Wagner [25].

4.3.5. Conductivity measurement

From the conductance data obtained from the LCR meter, the conductivity of the synthesized ceramics was calculated. The dependence of the conductance on temperature and frequency of different compositions of BCNTO is shown in Fig. 4.8. It is observed from

Fig. 4.8a that the sample shows semiconducting, observed at 10 kHz frequency. The activation energy was found to be 0.15 eV, 0.14 eV, and 0.11 eV for BCNTO-0.05, BCNTO-0.1, and BCNTO-0.2 ceramics respectively with the help of Arrhenius law.

The frequency-dependence of the conductivity obeyed the Johncher's power law [26];

$$\sigma(\omega)=\sigma_0+A\omega^s \quad (4.2)$$

Where A is a constant and s is the power-law exponent.

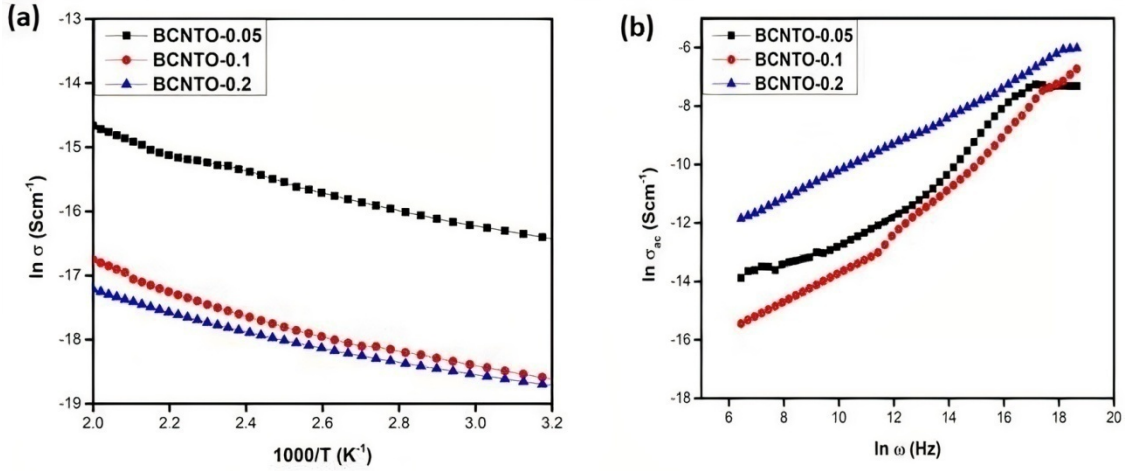

Fig. 4.8a Plots of Conductivity (ln σ) with the inverse of temperature at 10 kHz; **b** frequency dependence of AC conductivity at 310 K for BCNTO-0.05, BCNTO-0.1, and BCNTO-0.2 ceramics.

Fig. 4.8b shows the variation of conductivity with frequency observed at 310 K. It was concluded that the AC conductivity [27] mainly depends upon frequency. Fig. 4.8b shows the AC conductivity as the function of the frequency at a temperature of 310 K. With the help of power law, calculated slope s of ln σ_{ac} vs lnω was 0.81, 0.71, and 0.48 for BCNTO-

0.05, BCNTO-0.1, and BCNTO-0.2 ceramics respectively, which suggest the conduction in the material via the thermally activated process.

4.3.6. Electrochemical studies

There are two types of electrochemical capacitors based on electrochemical activities, i.e. electrical double-layer capacitors (EDLCs) and pseudocapacitors. EDLC based materials undergo surface adsorption-desorption during the charging-discharging (CD) and pseudocapacitive materials show redox behavior during the CD process [28]. The cyclic voltammetry (CV) testing was performed to find out the current response with the change in voltage. In the case of EDLC, the CV is rectangle or quasi-rectangle, but for pseudocapacitive materials, we get peaks due to redox processes.

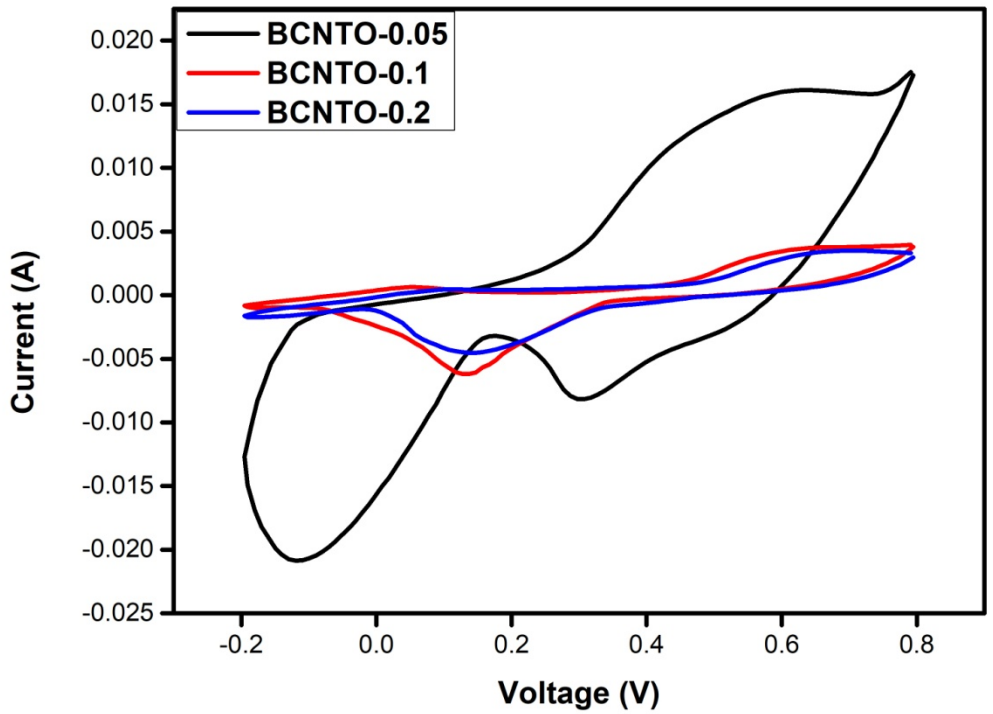

Fig. 4.9 Cyclic Voltammetry plot of BCNTO-0.05, BCNTO-0.1, and BCNTO-0.2 ceramics sintered at 1123 K for 8 h.

Fig. 4.9 demonstrates the CV curve of all the prepared electrodes. The maximum current was generated for BCNTO-0.05, but BCNTO-0.1 and BCNTO-0.2. The stable potential window was found to be 1 Volt. The calculated specific capacitances of BCNTO-0.05, BCNTO-0.1, and BCNTO-0.2 based electrodes are 71 F/g, 38 F/g, and 32 F/g, respectively indicating that they can be used to fabricate supercapacitors.

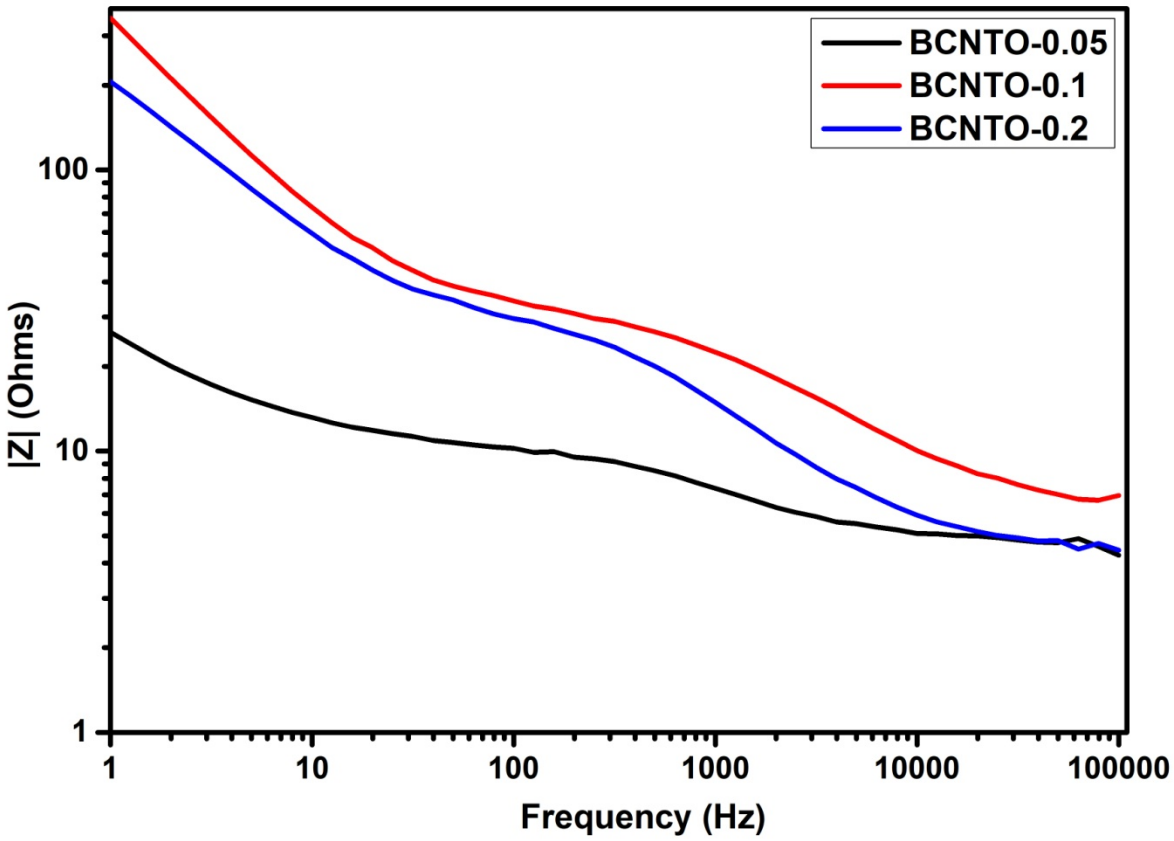

Fig. 4.10 Frequency dependence of real part of impedance of BCNTO-0.05, BCNTO-0.1, and BCNTO-0.2 ceramics.

From Fig. 4.10, it can be seen that the total impedance for all the BCNTO is decreasing with an increase in frequency, which tells that the material can be used for energy storage. The Nyquist plot has been given in Fig. 4.11.

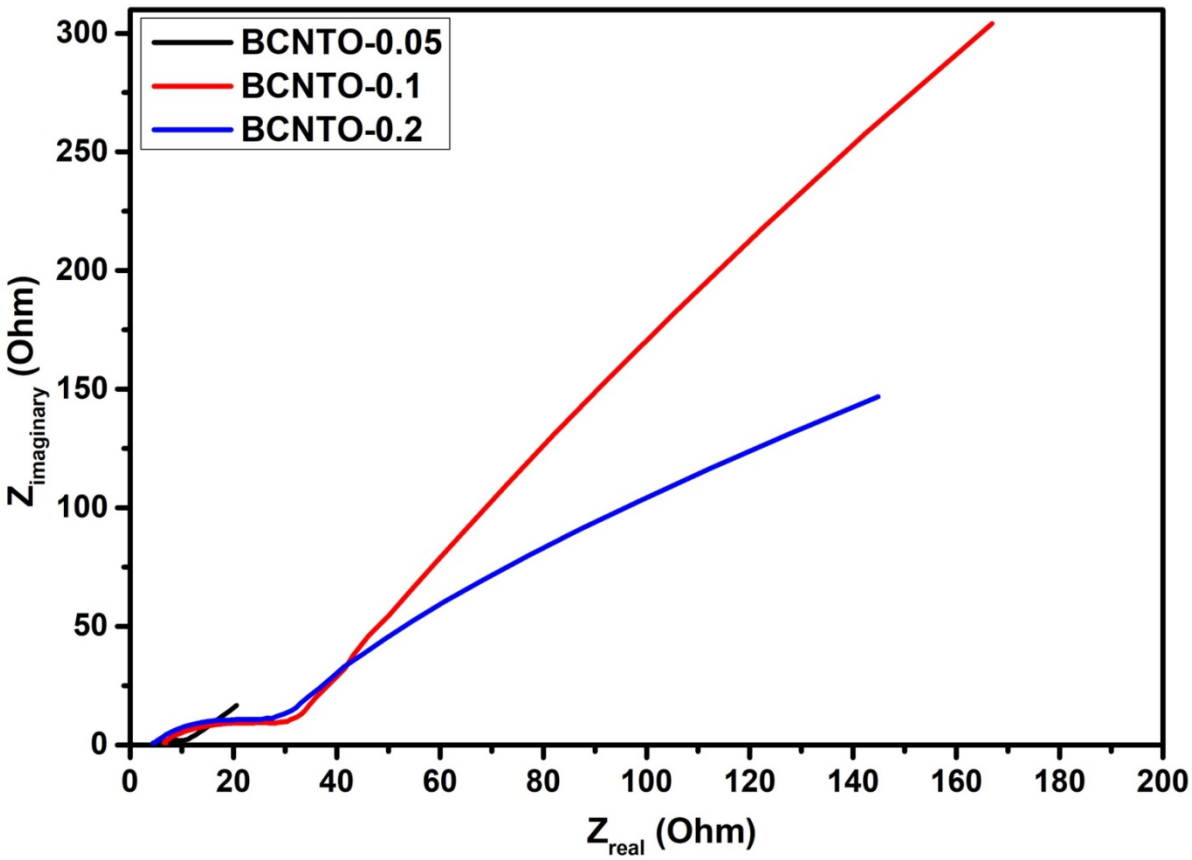

Fig. 4.11 Nyquist plot of BCNTO-0.05, BCNTO-0.1, and BCNTO-0.2 ceramics.

From the semicircle part, we have calculated charge transfer resistances by measuring their diameters. The calculated charge transfer resistances of BCNTO-0.05, BCNTO-0.1, and BCNTO-0.2 are 5 Ω, 27 Ω, and 27.7 Ω, respectively.

4.4. Conclusions

Ni-doped BCTO ceramics were synthesized by a chemical route at low temperatures. The single-phase formation of BCNTO ceramics was verified by XRD. There was a slight difference in sizes due to dopant concentration. The crystallite size of Ni-doped BCTO

ceramics was in the range of 42.07-42.10 nm. The particle size of BCNTO-0.2 ceramic (higher Ni-doped sample) was found to be 65.28 nm. The oxidation state was validated by XPS. As expected, a high value of dielectric constant (ε_r) was observed at a low-frequency range. However, low tangent losses were observed at high frequency. The dielectric constant for BCNTO-0.2 ceramic was found to be 1940 at 100 Hz frequency and 470 K temperature. For the BCNTO-0.2 ceramic, the tangent loss at 310 K temperature and 10 kHz frequency was 0.07.The conductivity of BCNTO ceramics increases with an increase in temperature supporting the Arrhenius law. AC conductivity of BCNTO ceramics increases with increasing frequency satisfying Johncher's power law. The charge transfer resistances of BCNTO-0.05, BCNTO-0.1, and BCNTO-0.2 are 5 Ω, 27 Ω, and 27.7 Ω, respectively.

References

1. Wu, X., Chen, X., Zhang, Q.M. and Tan, D.Q. (2022). Advanced dielectric polymers for energy storage. *Energy Storage Materials*, 44, 29-47.

2. Zhou, Y. and Wang, Q. (2020). Advanced polymer dielectrics for high temperature capacitive energy storage. *Journal of Applied Physics*, 127(24), 240902.

3. Zhang, H., Wei, T., Zhang, Q., Ma, W., Fan, P., Salamon, D., Zhang, S.T., Nan, B., Tan, H. and Ye, Z.G. (2020). A review on the development of lead-free ferroelectric energy-storage ceramics and multilayer capacitors. *Journal of Materials Chemistry C*, 8(47), 16648-16667.

4. Ghozza, M.H., Yahia, I.S. and El-Dek, S.I. (2020). Role of B-site cation on the structure, magnetic and dielectric properties of nanosized $La_{0.7}Sr_{0.3}Fe_{1-x}M_xO_3$ (M= Mn; Co and x= 0, 0.5) perovskites. *Materials Research Express*, 7(5), 056104.

5. Jiang, B., Iocozzia, J., Zhao, L., Zhang, H., Harn, Y.W., Chen, Y. and Lin, Z. (2019). Barium titanate at the nanoscale: controlled synthesis and dielectric and ferroelectric properties. *Chemical Society Reviews*, 48(4), 1194-1228.

6. Yao, K., Chen, S., Lai, S.C. and Yousry, Y.M. (2022). Enabling distributed intelligence with ferroelectric multifunctionalities. *Advanced Science*, 9(1), 2103842.

7. Kum-onsa, P., Chanlek, N., Takesada, M., Srepusharawoot, P. and Thongbai, P. (2021). (La^{3+} , Mg^{2+}) codoped $BiFeO_3$ nanopowders: Synthesis, characterizations, and giant dielectric relaxations. *Engineering and Applied Science Research*, 48(6), 766-772.

8. Liu, Z. and Yang, Z. (2017). Structure and Differentiated Electrical Characteristics of $M_{1/2}La_{1/2}Cu_3Ti_4O_{12}$ (M= Li, Na, K) Ceramics Prepared by Sol–Gel Method. *Journal of Electronic Materials*, 46, 6175-6187.

9. Jumpatam, J., Boonlakhorn, J., Phromviyo, N., Chanlek, N. and Thongbai, P. (2022). Electrical responses and dielectric properties of (Zn^{2+}, F^{-}) co–doped $CaCu_3Ti_4O_{12}$ ceramics. *Materialia*, 23, 101441.

10. Jumpatam, J., Putasaeng, B., Chanlek, N., Boonlakhorn, J., Thongbai, P., Phromviyo, N. and Chindaprasirt, P. (2021). Significantly improving the giant dielectric properties of $CaCu_3Ti_4O_{12}$ ceramics by co-doping with Sr^{2+} and F^{-} ions. *Materials Research Bulletin*, 133, 111043.

11. Rani, S., Ahlawat, N., Punia, R., Sangwan, K.M. and Khandelwal, P. (2018). Dielectric and impedance studies of La and Zn co-doped complex perovskite $CaCu_3Ti_4O_{12}$ ceramic. *Ceramics International*, 44(18), 23125-23136.

12. Wang, J., Lu, Z., Deng, T., Zhong, C. and Chen, Z. (2018). Improved dielectric, nonlinear and magnetic properties of cobalt-doped $CaCu_3Ti_4O_{12}$ ceramics. *Journal of the European Ceramic Society*, 38(10), 3505-3511.

13. Saîd, S., Didry, S., El Amrani, M., Autret-Lambert, C. and Megriche, A. (2018). Brilliant effect of Ni substitution in the appearance of high dielectric constant in $CaCu_{2.9}Ni_{0.1}Ti_{3.9}Ni_{0.1}O_{12}$ ceramics. *Journal of Alloys and Compounds*, 765, 927-935.

14. Wang, Y., Huang, X., Li, T., Li, L., Guo, X. and Jiang, P. (2019). Polymer-based gate dielectrics for organic field-effect transistors. *Chemistry of Materials*, *31*(7), 2212-2240.

15. Sharma, S., Singh, M.M. and Mandal, K.D. (2017). Magnetic and dielectric properties of a lanthanum-doped yttrium copper titanate ceramic. *New Journal of Chemistry*, 41(14), 6359-6370.

16. Domengès, B., Riquet, G., Marinel, S. and Harnois, C. (2020). High-resolution FIB-TEM-STEM structural characterization of grain boundaries in the high dielectric constant perovskite $CaCu_3Ti_4O_{12}$. *Journal of the European Ceramic Society*, 40(10), 3577-3584.

17. Rai, V.S., Pandey, S., Kumar, V., Verma, M.K., Kumar, A., Singh, S., Prajapati, D. and Mandal, K.D. (2021). Investigation of microstructure and dielectric behavior of $Bi_{2/3}Cu_{3-x}Mg_xTi_4O_{12}$ (x= 0, 0.05, 0.1 and 0.2) ceramics synthesized by semi-wet route. *Journal of Materials Science: Materials in Electronics*, 32, 7671-7680.

18. Prajapati, D., Rai, V.S., Pandey, S., Kumar, V., Verma, M.K., Kumar, A., Singh, S., Sahoo, K. and Mandal, K.D. (2021). Studies of microstructural, dielectric, and impedance spectroscopic properties of $Bi_{0.617}Y_{0.05}Cu_3Ti_4O_{12}$ ceramic synthesized through semi-wet route. *Journal of Materials Science: Materials in Electronics*, 32, 26371-26383.

19. Sahu, M. and Choudhary, R.N.P. (2019). Processing and Electrical Characteristics of Barium Doped $CaCu_3Ti_4O_{12}$. *Transactions on Electrical and Electronic Materials*, 20, 16-23.

20. Gaâbel, F., Khlifi, M., Hamdaoui, N., Beji, L., Taibi, K. and Dhahri, J. (2019). Microstructural, structural and dielectric analysis of Ni-doped $CaCu_3Ti_4O_{12}$ ceramic with low dielectric loss. *Journal of Materials Science: Materials in Electronics*, 30, 14823-14833.

21. Ghafoor, A., Bibi, I., Ata, S., Majid, F., Kamal, S., Iqbal, M., Iqbal, S., Noureen, S., Basha, B. and Alwadai, N. (2021). Energy band gap tuning of $LaNiO_3$ by Gd, Fe and Co ions doping to enhance solar light absorption for efficient photocatalytic degradation of RhB dye: A mechanistic approach. *Journal of Molecular Liquids*, 343, 117581.

22. Nagamuthu, S., Zhang, Y., Xu, Y., Sun, J., uz Zaman, F., Denis, D.K., Hou, L. and Yuan, C. (2022). Non-lithium-based metal ion capacitors: recent advances and perspectives. *Journal of Materials Chemistry A*, 10(2), pp.357-378.

23. Mohammed, J., Bhargava, R., Khan, S., Mishra, S., Godara, S.K. and Srivastava, A.K. (2020). Crystal structure refinement, optical properties, dielectric response, and impedance spectroscopy of Ni^{2+-}, Co^{2+} substituted bismuth copper titanate (BCTO). *Materials Chemistry and Physics*, 248, 122933.

24. Kumar, V., Pandey, S., Kumar, A., Verma, M. K., Singh, S., Rai, V.S., Prajapati, D., Das, T., Sharma, A., Prajapat, C. L. and Gangwar, A. (2020). Investigation of dielectric, magnetic and impedance spectroscopic properties of $CaCu_{3-X}Mn_XTi_{4-X}Mn_XO_{12}$ (X= 0.10) nano-ceramic synthesized through semi-wet route. *Journal of Materials Research and Technology*, 9(6), 12936-12945.

25. Choi, H.J., Jung, Y.S., Han, J. and Cho, Y.S. (2020). In-situ stretching strain-driven high piezoelectricity and enhanced electromechanical energy-harvesting performance of a ZnO nanorod-array structure. *Nano Energy*, 72, 104735.

26. Javed, M., Khan, A.A., Kazmi, J., Mohamed, M.A., Khan, M. N., Hussain, M. and Bilkees, R. (2021). Dielectric relaxation and small polaron hopping transport in sol-gel-derived $NiCr_2O_4$ spinel chromite. *Materials Research Bulletin*, 138, 111242.

27. Yu, K., Tian, Y., Gu, R., Jin, L., Ma, R., Sun, H., Xu, Y., Xu, Z. and Wei, X. (2018). Ionic conduction, colossal permittivity and dielectric relaxation behavior of solid electrolyte $Li_{3x}La_{2/3-x}TiO_3$ ceramics. *Journal of the European Ceramic Society*, 38(13), 4483-4487.

28. Das, T. and Verma, B. (2020). Polyaniline-Acetylene black-Copper cobaltite based ternary hybrid material with enhanced electrochemical properties and its use in supercapacitor electrodes. *International Journal of Energy Research*, 44(2), 934-949.